Spin-lattice-charge coupling in quasi-one-dimensional spin-chain $NiTe_2O_5$

Ajay Tiwari,[1] D. Chandrasekhar Kakarla,[1,*] G. Macam,[1] C. H. Hsu,[1,2] F. C. Chuang,[1] H. C. Wu,[1] T. W. Kuo,[1] Arkadeb Pal,[1,3] H. Chou,[1] D. P. Gulo,[4] H. L. Liu,[4] Y. C. Chuang,[5] Y. C. Lai,[5] C. A. Lee,[3,6] Mitch M. C. Chou,[3,6] and H. D. Yang[1,3,†]

[1]*Department of Physics, National Sun Yat-sen University, Kaohsiung 80424, Taiwan*
[2]*Physics Division, National Center for Theoretical Sciences, Taipei 10617, Taiwan*
[3]*Center of Crystal Research, National Sun Yat-sen University, Kaohsiung 80424, Taiwan*
[4]*Department of Physics, National Taiwan Normal University, Taipei 11677, Taiwan*
[5]*National Synchrotron Radiation Research Centre, Hsinchu 30076, Taiwan*
[6]*Department of Materials and Optoelectronic Science, National Sun Yat-sen University, Kaohsiung 80424, Taiwan*

(Received 12 December 2021; accepted 6 April 2022; published 21 April 2022)

A high-quality $NiTe_2O_5$ single crystal was grown via the flux method and characterized using synchrotron x-ray diffraction (XRD) and electron probe microscopy techniques. The dc magnetization (M) confirms the antiferromagnetic long-range ordering temperature (T_N) at 28.5 K. An apparent domelike dielectric anomaly near T_N, with scaling of magnetodielectric (MD) coupling with magnetization (MD% $\propto M^2$), signifies higher-order magnetoelectric (ME) coupling. The critical finding is that magnetoelastic coupling plays a pivotal role in bridging the electrical and magnetic dipoles, which was further confirmed by temperature-dependent XRD. In addition, the theoretical charge density difference maps indicate that the emergence of electrical dipoles between the Ni and O atoms below T_N originates through *p-d* hybridization. Thus, the *p-d* hybridization-induced magnetoelastic coupling is considered a possible mechanism for the higher-order ME effect in this quasi-one-dimensional spin-chain $NiTe_2O_5$.

DOI: 10.1103/PhysRevMaterials.6.044409

I. INTRODUCTION

Low-dimensional spin systems have attracted a flurry of research interest owing to their rich quantum magnetic phenomena under external perturbations and are anticipated to have key applications in quantum computation [1–4]. One-dimensional spin-chain systems with low-spin-state compounds with spin $S = 1/2$ or $S = 1$ are interesting for quantum magnetism [5,6]. For example, low-dimensional Ni and Cu-based compounds exhibit interesting quantum physical states including Bose-Einstein condensation, spin liquids, spin ice, quantum multiferroics, and spin-flip-induced ferroelectrics [1,3,4,6–10]. Dimensionally restricted crystal growth in some compounds stabilizes in unique spin-frustrated lattices such as kagome, honeycomb, triangular, and pyrochlore. These lattices are the central point for obtaining the noncollinear spin-induced multiferroic behavior via the Dzyaloshinskii-Moriya interaction (DMI) [3,9,11–13]. Geometrically frustrated lattices and ferroelectricity induced by DMI have been highlighted over the years in multiferroic research. Despite this, many examples show that simple collinear spin arrangements invoke spin-induced multiferroicity either via the exchange-striction mechanism or by the simple spin-flip (flop) process [14–16]. $Ca_3Co_{2-x}Mn_xO_6$ is a classic example of an Ising collinear spin-chain-induced multiferroic system [17,18]. Theoretical and experimental investigations revealed the unique ↑↑↓↓ spin-configuration-induced multiferroicity via the exchange-striction mechanism [17]. Strong ME coupling and spin-induced multiferroic behavior were observed in the Haldane spin-chain system Tb_2BaNiO_5 [16]. Giant spin-flip-induced magnetoelectricity has been reported in several polar and nonpolar magnets, such as $Fe_2Mo_3O_8$ and $Cu_3Bi(SeO_3)_2O_2Cl$ [19,20]. These systems rule out the need for a noncollinear magnetic texture for spin-induced multiferroicity. Indeed, a linear antiferromagnetic/ferromagnetic (AFM/FM) spin chain is sometimes adequate to obtain spin-flip-induced ME or magnetoelastic coupling [19,21].

Recently, several strategies have been employed to chemically synthesize low-dimensional magnetic systems. Oxides with lone-pair ions or oxyhalides with a combination of lone-pair and electronegative anions act as chemical scissors to prevent bond formation [22]. In this respect, tellurium-based crystal systems exhibit extraordinary diversity due to flexible oxidation states along with a wide range of coordination geometries [22]. In particular, constituents of the NiO-TeO_2 binary phase diagram have received significant research interest due to their magnetic properties. As shown in Table I, magnetic interactions in many of the compounds exhibit either low-dimensional or spin-frustrated lattices along with lone-pair Te^{4+} ions, a plausible way to explore the spin-induced multiferroic behavior. Ni_3TeO_6 is a well-known polar noncentrosymmetric multiferroic with an AFM ordering temperature below (T_N) 52 K, crystallizing in the hexagonal crystal

*chandu@mail.nsysu.edu.tw
†yang@mail.nsysu.edu.tw

TABLE I. List of materials synthesized from NiO-TeO_2 binary phase diagram and their structural and magnetic ordering temperatures.

S.N.	Sample	Structure	Space group	T_N/T_C (K)	Dielectric anomaly T_D (K)	Reference
1.	$NiTeO_3$	Orthorhombic	*Pnma*	$T_C = 125$	?	[26–28]
2.	$NiTeO_4$	Monoclinic	$P2_1/c$	$T_N = 76$	?	[29]
3.	$NiTe_2O_5$	Orthorhombic	*Pbnm*	$T_N = 30$	28.5[a]	[30], this work
4.	Ni_3TeO_6	Trigonal	*R*3	$T_N = 52$	52	[23]
5.	$Ni_2Te_3O_8$	Monoclinic	*C*2/*c*	$T_N = 35$	?	[24]
6.	$NiTe_6O_{13}$	Trigonal	$R\bar{3}$	?	?	[25]

aReported in this work.

structure and *R*3 space group [23]. The crystal structure indicates three crystallographically inequivalent Ni^{2+} ions with linear spin chains of the $\uparrow\uparrow\downarrow\downarrow$ spin configuration along the hexagonal *c*-axis [23]. Recently, experimental results have explored the field-induced metamagnetic transitions and associated nonhysteretic colossal ME effects in Ni_3TeO_6. The origin of the spin-induced electric polarization is attributed to symmetric exchange striction along the Ni chains in the *c* direction [23]. In addition, $Ni_2Te_3O_8$ and $NiTe_6O_{13}$ are antiferromagnetically ordered at low temperatures with Ni^{2+} zigzag chain arrangements [24,25]. $NiTeO_3$ exhibits weak ferromagnetism with a transition temperature of approximately $T_C = 120$ K, where $Te^{4+}O_6$ is an active stereochemical ion [26–28]. $NiTeO_4$ shows excellent performance in battery applications owing to its unique Jahn-Teller Ni^{2+} ion [29].

Although Ni_3TeO_6 was a well-established polar multiferroic, very little is known about other compounds from the NiO-TeO_2 family. After the polar multiferroic Ni_3TeO_6, $NiTe_2O_5$ also received interest from the NiO-TeO_2 family because of its complex spin structure with a quasi-one-dimensional spin chain [30]. $NiTe_2O_5$ is stabilized in the orthorhombic *Pbnm* space group with a long-range AFM transition at $T_N = 30.5$ K [30]. Despite its quasi-one-dimensional $S = 1$ spin chain, unconventional critical behavior has been recently explored through magnetic and neutron measurements [30]. The low-temperature spin structure shows an interesting Ising-like spin configuration with FM magnetic moments along the spin-chain direction coupled AFM with the adjacent spin-chain forming a three-dimensional (3D) AFM ground state. Due to the distortion of the NiO_6 octahedral, the magnetic moments are tilted away from the *c*-axis, bringing a finite component of longitudinal magnetic moments in the *bc* plane. The *bc* plane has a unique square lattice with net magnetic moment along $\pm a$-axis whose spin orientation alternates in every two layers and forms the AFM $\uparrow\uparrow\downarrow\downarrow\uparrow\uparrow\cdots$ pattern along the *c*-axis. Surprisingly, ^{125}Te nuclear magnetic resonance (NMR) studies in the paramagnetic region unveil intricate magnetic correlations between spin-chain and square-planar lattices well above the T_N [31]. Ising-like easy-axis magnetic correlations persist in the spin chain in the paramagnetic zone, with dominant spin fluctuations appearing in the square lattice [31]. This unusual magnetic behavior can be explained via the self-hole doping effect that led to strong spin-charge coupling much above its magnetic exchange energy scales [31]. Conceding its unique spin structure with longitudinal and transverse components makes it a promising candidate for exploring dielectric and MD behavior. This article presents a comprehensive study of $NiTe_2O_5$ through structural, magnetic, and dielectric measurements. Consequently, this study demonstrates, $NiTe_2O_5$ has peculiar properties with *p-d* hybridization-induced strong spin-lattice-charge coupling that results in a dielectric anomaly at T_N with higher-order magnetoelectric effect.

II. EXPERIMENTAL DETAILS

A. Sample synthesis

Single crystals and polycrystals of $NiTe_2O_5$ have been synthesized by flux and solid-state methods, respectively [30,32]. For the $NiTe_2O_5$ single-crystal growth, high-purity NiO (Alfa Aesar, 99.995%) and TeO_2 (Alfa Aesar, 99.999%) powders were mixed in the air at a concentration of 5 M and a molar ratio of 1:4. This sample solution was loaded into flat-bottom quartz ampoules of length 10 cm and diameter 25 mm, which were placed vertically into a box furnace with the help of a large-diameter Al_2O_3 crucible and heated at a rate of 3 °C/min up to the melting point, as shown in Fig. S1 in the Supplemental Material [33]. For the growth of $NiTe_2O_5$ single crystals, the optimum temperatures were set at 900 °C–700 °C for 8 days with prolonged cooling followed by shutdown of the furnace at 700 °C. Light-green color $NiTe_2O_5$ single crystals along with the white powder residue of TeO_2 appeared at the bottom of the ampoule, and $NiTe_2O_5$ crystals were selected or removed by dipping this in a 3 M KOH solution along with very slow ultrasonication to remove the white powder. Using this method, $NiTe_2O_5$ single crystals were obtained with a length of 3–5 mm. The electron probe microanalysis (EPMA) method was employed to determine the elemental composition of all heavy elements in the synthesis of $NiTe_2O_5$ single crystals which is shown in Fig. S2, and Tables S3 and S4 [33].

B. Experimental characterizations and theoretical calculation

The quality of the $NiTe_2O_5$ single crystals and polycrystals was checked at room temperature using high-resolution synchrotron x-ray diffraction (SXRD) with the 09A beamline of the Taiwan Photon Source (TPS 09A) at the National Synchrotron Radiation Research Center (NSRRC), Taiwan. In the SXRD measurements, the $NiTe_2O_5$ single crystals were crushed into a fine powder, and the sample was loaded into a quartz capillary of 0.3 mm diameter. The data were collected using reflection geometry with a wavelength of $\lambda = 0.774\,89$ Å and a double-crystal monochromator Si (111) with

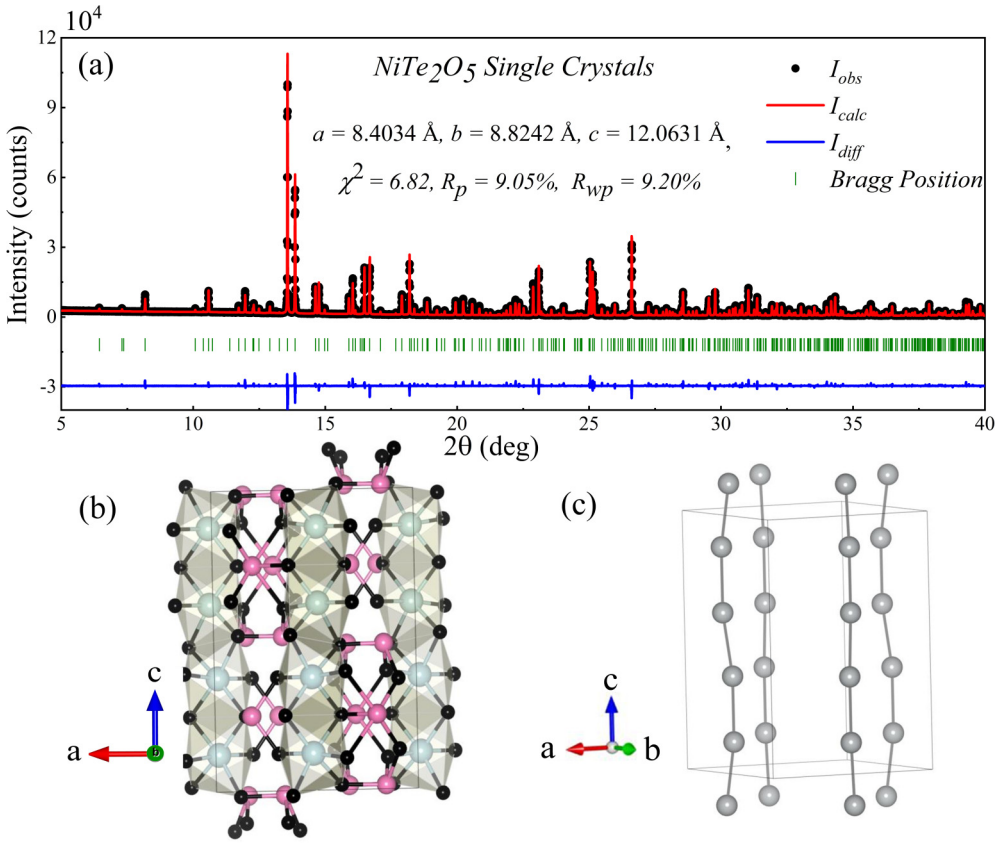

FIG. 1. (a) Rietveld refinement of room-temperature high-resolution synchrotron x-ray diffraction of powdered $NiTe_2O_5$ single crystals; (b) the crystal structure of $NiTe_2O_5$ in the *ac* plane in which the Ni^{2+} is represented by silver color octahedra in the *c*-axis direction with NiO_6 atomic arrangement and Te^{4+} is shown in pink color and oxygen is in black; (c) Ni^{2+} atomic arrangement in the *c*-axis direction.

an energy resolution of 1.33×10^{-4}. Diffraction data were collected in the 2 °–120 ° range in steps of 0.004 °. Rietveld refinement of the SXRD data was performed using FULLPROF suite software. The crystal structure and variation in bond lengths were analyzed using VESTA (version 3.5.2) software through the VESTA file obtained from the refinement. For low-temperature XRD, the Bruker AXS, D8 advanced x-ray diffractometer was used from 300 to 12 K. A flat-faced single crystal of approximately 2 mm × 2 mm × 1 mm was chosen for the dielectric measurements. Silver paint was employed as electrodes on both sides of the crystal to form a parallel-plate capacitor. Dielectric (ε_r') measurements were performed using an Agilent E4980A precision LCR meter with an excitation ac voltage of 10 V. Temperature- and field-dependent dielectric measurements were performed with a homemade sample probe in a Quantum design MPMS system. All magnetic measurements were conducted using a magnetic property measurement system (MPMS-XL7) with a magnetic field up to 7 T. First-principles calculations were based on density functional theory [34] as implemented in the Vienna *Ab Initio* Simulation Package (VASP) [35,36] with a plane-wave basis and the projector augmented wave method [37]. The generalized gradient approximation in the Perdew-Burke-Ernzerhof [38] functional form of the exchange-correlation functional was adopted with a cutoff energy of 400 eV. The experimental lattice constants were used, and the atomic positions were relaxed until the residual forces acting on each atom were not greater than 10^{-3} eV/Å. The self-consistent convergence criterion for electronic structures was set to 10^{-6} eV.

III. RESULTS AND DISCUSSION

A. Structural analysis

The room-temperature SXRD with Rietveld refinement for crushed $NiTe_2O_5$ single crystals is shown in Fig. 1(a). The SXRD reflections were refined using the *Pbnm* space group, without any noticeable secondary phases. Structural parameters such as atomic positions, lattice constants, and goodness of fit are summarized in the Supplemental Material, Table S1 [33], and are consistent with a previously published report [30]. The pictorial representation of the crystal structure drawn with the VESTA software illustrates the one-dimensional distorted corner-connecting NiO_6 chains formed along the *c*-axis direction, as shown in Figs. 1(b) and 1(c). The magnetic interaction between the Ni^{2+} ions occurs via two oxygen atoms within the chain. The lone-pair Te^{4+} ions bridged the interchain Ni^{2+} magnetic interactions. From the crystallographic point of view, the intrachain (6.1 Å) and interchain (2.8 Å) Ni^{2+}-Ni^{2+} distances indicate possible one-dimensional magnetic behavior. Further presence of lone-pair Te^{4+} ions between the interchain Ni^{2+}-Ni^{2+} magnetic interaction is expected to modulate the electrical properties at the one site of magnetic interactions. For comparison, Rietveld

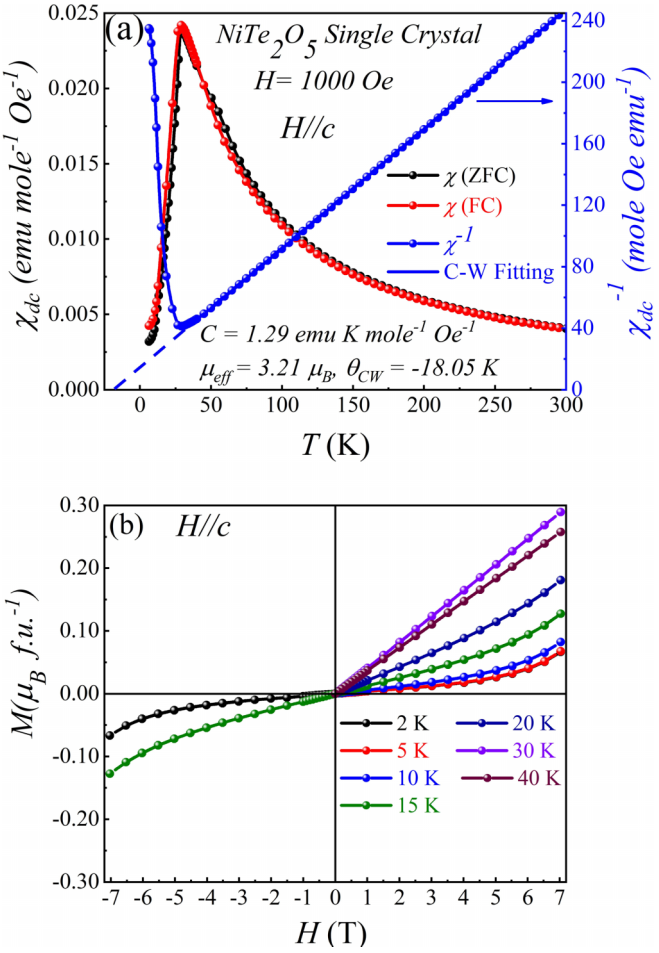

FIG. 2. (a) The ZFC-FC susceptibility (right y axis) and inverse susceptibility (left y axis) of $NiTe_2O_5$ single crystal approximately in the $H//c$ direction. (b) Depiction of the isothermal M vs H curve at different temperatures from 2 to 40 K of $NiTe_2O_5$ single crystal approximately in the $H//c$ direction.

refinement of $NiTe_2O_5$ polycrystals was also performed, and the results are shown in Table S2 and Fig. S3(a) [33].

B. Magnetic property

The T dependence of zero-field cooled (ZFC) and field-cooled (FC) magnetic susceptibility ($H//c$ axis) for the $NiTe_2O_5$ single crystal for $H = 1000$ Oe is displayed in Fig. 2(a). As shown in Fig. 2(a), the ZFC and FC magnetization increase with decreasing T and exhibit a sharp transition characteristic of long-range AFM ordering at $T_N \sim 28.5$ K. Despite the small difference in T_N value, the nature and magnitude of M along with the $H//c$ axis is consistent with published magnetic data indicating that the Ni^{2+} magnetic spin preferentially aligns along the c-axis [30]. The effective paramagnetic moment was estimated using the Curie-Weiss (CW) law [$\chi = C/(T - \theta_{CW})$]; here θ_{CW} is the Curie temperature. The obtained negative $\theta_{CW} \sim -18.05$ K further signifies the robust AFM interactions. The calculated effective paramagnetic (PM) moment through the equation $\mu_{eff} = \sqrt{3K_BC/N_A} \sim 3.21\ \mu_B$ for the octahedrally coordinated Ni^{2+} is slightly higher than the spin-only magnetic contribution of Ni^{2+} ions ($\mu_{eff} = g\mu_B\sqrt{S(S+1)} = 2.82\ \mu_B$; g and $S = 1$) and lower than the total angular moment ($g\mu_B\sqrt{j(j+1)} = 5.59\ \mu_B$; $g = 5/4$ and $S = 4$). A similar high PM μ_{eff} has been observed in several other Ni-based magnetic systems, which hints at finite spin-orbit coupling [39–41]. A similar feature was observed for the polycrystalline samples presented in Supplemental Material, Fig. S3(b) [33].

To further examine possible metamagnetic transitions, isothermal magnetization was performed from 2 to 40 K to examine a possible spin transition. As shown in Fig. 2(b), M at low H increases linearly and shows enhancement starting from 4 T and does not exhibit saturation even up to 7 T, indicating possible metamagnetic/spin-flip transition above 7 T. Interestingly, the onset of metamagnetic transition matched with Ni_3TeO_6, where spin-induced polarization appeared [23]. The metamagnetic onset was progressively suppressed with increasing temperature, and linearity was observed when approaching T_N. An ultrahigh-field magnetization measurement ($H > 7$ T) was required to unveil the nature and temperature evolution of the metamagnetic transition, which is beyond the scope of this study.

C. Dielectric and magnetodielectric coupling

$NiTe_2O_5$ is an insulator at 300 K, with T_N at 28.5 K, which makes it a promising candidate for the investigation of dielectric (ε_r') properties and magnetodielectric measurements. The ε_r' vs T ($E \perp c$) was performed from 4 to 60 K at a constant frequency of 1 MHz for $NiTe_2O_5$ single crystals, as shown in Fig. 3(a). For comparison, ε_r' vs T measurements were performed on the polycrystalline samples at different frequencies and are presented in Fig. S4(a) [33]. With the decrease in T, ε_r' decreases linearly and shows a domelike dielectric anomaly ($T_D = 28.5$ K) near $T_N = 28.5$ K. It is important to note that a similar domelike ε_r' vs T curve is observed even for the polycrystalline samples shown in Fig. S4(a) [33]. The robust nature of this transition (polycrystalline and single crystals) indicates its intrinsic dielectric nature. The ε_r', loss $\tan\delta$ values, and frequency-independent dielectric anomalies suggest that this could be related to the lattice contribution of the dielectric anomaly [42–44]. The deviation from the lattice contribution of a dielectric anomaly at magnetic ordering temperatures has been discussed in several systems and is usually expressed using the following formula:

$$\varepsilon_r'(T) = \varepsilon_r'(0) + \frac{A}{[\exp(T^*/T) - 1]},$$

where A is a constant and $T^* = h\upsilon_T/k_B$ represents the characteristic temperature associated with the transverse phonon mode frequency (υ_T); a satisfactory fit to the experimental data above T_D is seen in Fig. 3(a), and the observed lattice dielectric constant deviates near the T_N. The obtained fitting parameters lead to a υ_T of 29.23 cm^{-1} and this value is one order of magnitude smaller than for well-known AFM MnO and MnF_2 piezomagnet systems [45–47].

To further check the influence of H on the ε_r', ε_r' vs H ($H//c$) data were studied at 2 K. Clearly, a significant MD (~0.7%) has been noticed in fields up to 7 T. Interestingly, almost zero MD was maintained for the moderate magnetic fields (~4 T), and thus a jump in the MD was observed, and

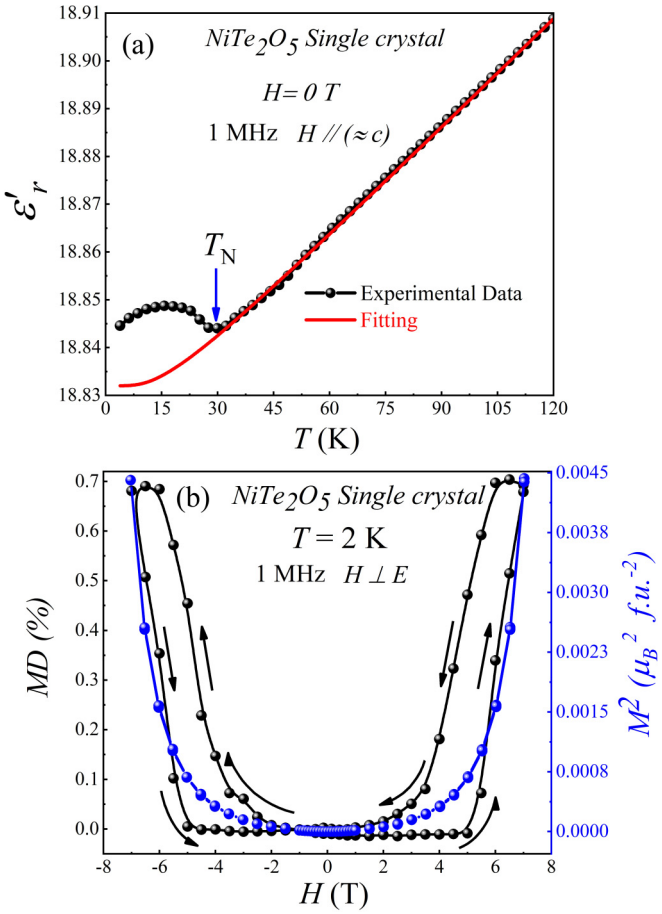

FIG. 3. (a) Shows ε_r' vs T from 5 to 50 K of (a) $NiTe_2O_5$ single crystals at 1 MHz and 0 T magnetic fields with a clear dielectric anomaly at Néel temperature (T_N) which is around 28.5 K, along with the fitting of dielectric constant for lattice contribution which is shown in red color. (b) Shows the magnetodielectric coupling percentage MD (%) (MD (%) $= \{[\varepsilon_r'(H) - \varepsilon_r'(0)]/\varepsilon_r'(0)\} \times 100$) vs H (right axis) and M^2 vs H (left axis) curves at 2 K and 1 MHz frequency; a clear correspondence between magnetization and dielectric change has been noticed.

this feature is symmetric in the negative direction, as shown in Fig. 3(b). This rules out the possibility of temperature drift or artifact effects on the observed MD. Further, an apparent hysteresis between the MD curves has been noted for the magnetic field ramp up and down directions; at present, there is no clear explanation for this behavior. To correlate the MD behavior with the magnetization changes, the M^2 vs H curve is plotted. This was observed to be paraboliclike, where the onset of the M^2 rise occurred almost near the MD rise. It is interesting to mention that this is closely related to the onset of the metamagnetic transition. Similar metamagnetic-transition-driven MD or multiferroic behaviors have been observed in several systems, such as $Cu_9O_2(SeO_3)_4Cl_6$ and Pb_2MnO_4 [48,49]. The M^2 vs MD scaling has been linked to the higher-order ME coupling in well-established multiferroic and nonmultiferroic systems and can be ascribed to magnetoelastic coupling [50–53]. A similar MD variation was noted in ε_r' vs T measurements at different H values for the polycrystalline $NiTe_2O_5$ sample, as shown in Fig. S4(b) [33].

D. T-dependent XRD

To elucidate the origin of the higher-order ME coupling, the T-dependent XRD of $NiTe_2O_5$ (crushed single crystals) was carried out in the temperature window of 300–10 K shown in Fig. 4(a). To check the crystal symmetry with the change of T, a Rietveld refinement measurement has been carried out at different T. Orthorhombic *Pbnm* crystalline symmetry was preserved without any global structural transformation from 300 to 10 K. However, local crystalline changes were observed, where some of the XRD reflections initially shifted to higher 2θ, and below T_N, they began shifting to the lower 2θ side as seen in Fig. 4(b). Despite this, the system still maintained *Pbnm* symmetry even at 10 K. To evaluate the local crystal changes (lattice parameters and bond lengths), a T-dependent lattice parameter from the Rietveld fits is presented in Fig. 4(c). As expected, all the lattice parameters, including the unit cell volume, decreased with T. However, anomalies in the lattice parameters were noted near T_N, where a slope change appeared in the positive thermal expansion. With a further decrease in T, a positive to negative thermal expansion was observed at 12 K. The feature appeared to have an inverted domelike structure. This result indicates that the elastic changes at the T_N signify the magnetoelastic coupling that collaborates with the changes in the lattice dielectric constant.

E. Theoretical interpretation for higher-order magnetoelectric coupling

Our experimental measurements show that $NiTe_2O_5$ exhibits magnetodielectric coupling, wherein the occurrence of a dielectric anomaly coincides with the onset of long-range magnetization at $T_N = 28.5$ K. Such observations may indicate magnetoelectric coupling, which may occur because of one or more of the following mechanisms [54]: lone-pair [55], exchange-striction, charge ordering/transfer, geometrical spin-frustration, and spin-driven mechanisms [18,56].

We performed first-principles calculations to shed light on the mechanism underlying the interplay of the electrical and magnetic properties of $NiTe_2O_5$. Using the experimentally measured low-temperature lattice parameters, we calculated the energies of the FM, nonmagnetic (NM), and canted AFM magnetic configurations of the low-temperature structure, as shown in Table II. This shows that the canted AFM is lower in energy than the FM and NM states by 0.1216 and 5.5 eV, respectively. The spin distribution of the canted AFM illustrated in Fig. 5(a) shows a one-dimensional magnetic chain (along the z-direction) with counterpropagating adjacent spin-chains leading to zero net magnetization. Spin-orbit coupling (SOC) effects induced the canting of the magnetic moments and slightly widened the energy band gap (see Supplemental Material, Fig. S5 [33]), which is consistent with the published spin structure [30]. The calculated local magnetic moments for Ni atoms have a large m_z component of 1.523 μ_B canted from the c-axis that led to m_x and m_y components of magnetic moments 0.018 μ_B and 0.057 μ_B, respectively.

To understand the effect of magnetism on the electronic properties, we calculated the charge density difference between NM and canted AFM states, defined as $\delta_\rho = \rho_{AFM} - \rho_{NM}$. Figure 5(b) shows that the majority of the charge density

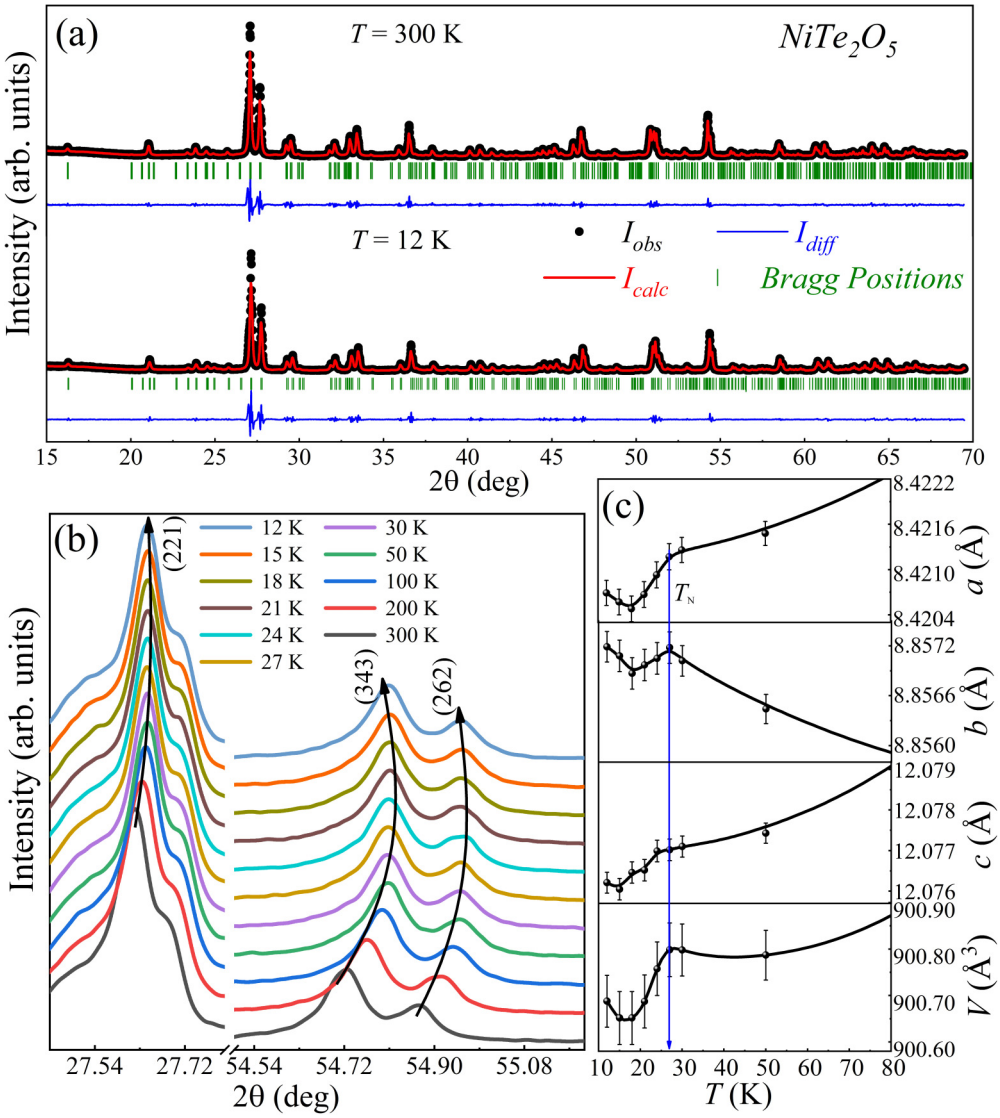

FIG. 4. (a) Temperature-dependent x-ray diffraction pattern with Rietveld refinement of $NiTe_2O_5$ powdered sample at 12 and 300 K. From the low-temperature and room-temperature XRD pattern it is evident that there is no global crystal structural change in $NiTe_2O_5$. (b) Shows the deviation of the highest peak with the plane (221) and higher angle peaks (2θ) with the plane (343) and (262) by decreasing the temperature of the $NiTe_2O_5$ powdered sample from 300 to 12 K. As the temperature decreases from 300 K, the peaks shift toward the higher 2θ angles until 27 K, which is very near to the T_N (28.5 K) and beyond 27 K the peaks start shifting toward the lower 2θ angles side. (c) After the Rietveld refinement at all temperatures the lattice parameters (a, b, and c) and unit cell volume (V) of the $NiTe_2O_5$ powdered sample have been plotted, and it is clear from the plot that there is variation in lattice parameters and unit cell volumes below the T_N. These results suggest that there is some magnetostriction phenomenon present in the $NiTe_2O_5$ sample below T_N without any global crystal structural change which may trigger the dielectric, magnetic transitions at 28.5 K.

distribution is clustered around the NiO_6 octahedra. We can distinguish oxygen atoms according to their location in the unit cell as (1) bonded within the NiO_6 octahedra and (2) non-bonded within the NiO_6 octahedra. Quantitatively, the average charge difference between the NM and canted AFM states for the case when an O atom bonded within the octahedra gain charges is $-0.023\,e$, for the nonbonded O atom it is $-0.003\,e$, and for Ni atom when it loses charges it is $0.066\,e$. Further,

TABLE II. SOC energies, net magnetic moments, and local magnetic moments of low-temperature $NiTe_2O_5$ with nonmagnetic (NM), FM, and AFM configurations.

12 K	SOC energy (eV)	Net magnetic moment (μ_B)	Local magnetic moment (μ_B)
FM	−353.064	0.0000 0.0000 15.9713	$m_x = m_y = 0.0$, $m_z = 1.547$
NM	−347.687	0.0000 0.0000 −0.0000	$m_x = m_y = m_z = 0.00$
AFM	−353.185	−0.0000 0.0000 −0.0000	$m_x = \pm 0.018$, $m_y = \pm 0.057$, $m_z = \pm 1.523$

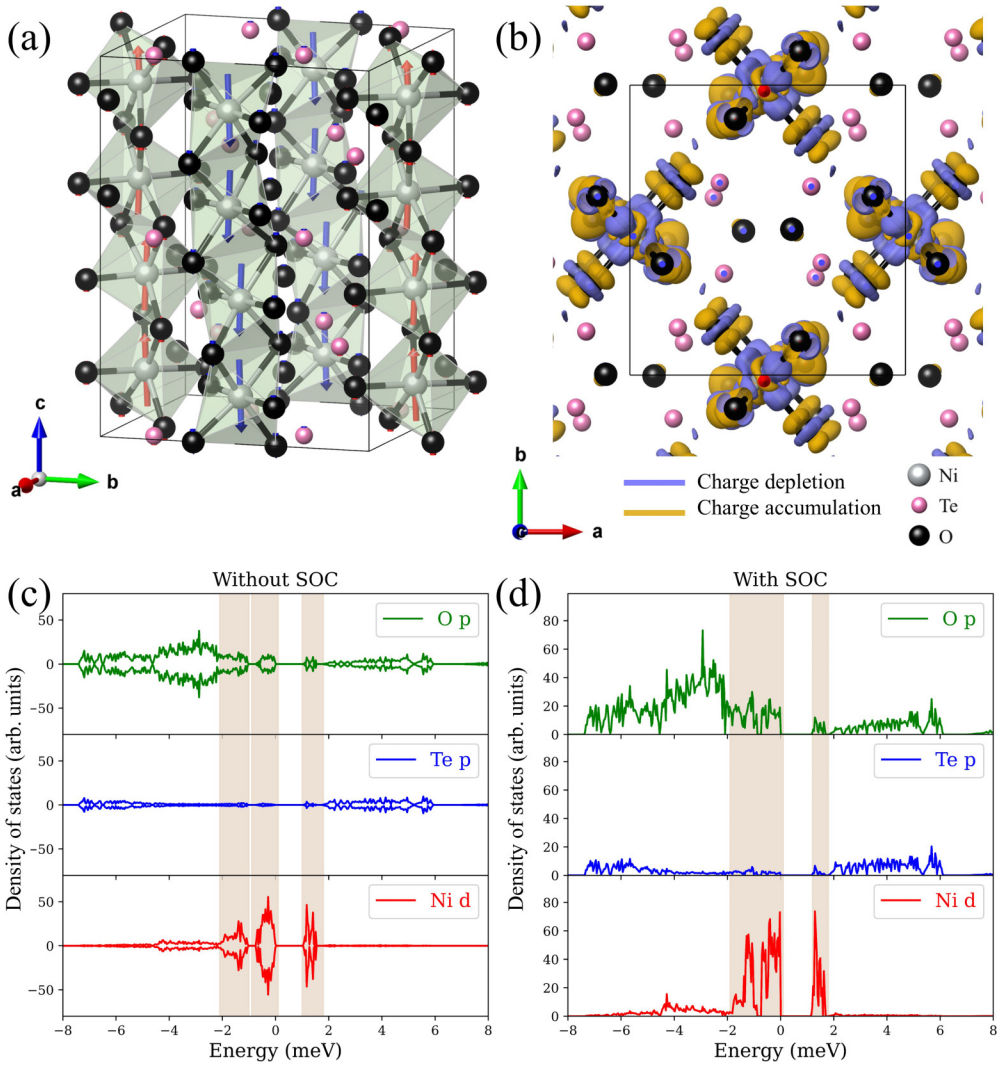

FIG. 5. (a) Spin distribution and (b) charge density difference ($\rho_{\mathrm{AFM}} - \rho_{\mathrm{NM}}$) of $NiTe_2O_5$. The spin-up and spin-down channels are indicated by red and blue arrows, respectively. The charge distribution is visualized using the isosurface value of 0.001 15 e Å^{-3}. The density of states of AFM $NiTe_2O_5$ (c) without and (d) with spin-orbit coupling (SOC).

Table III quantifies the charge transfer values for the unit cell's Ni and O oxygen atoms within NiO_6 octahedra. Thus, most of the electric charge transfer occurred between the oxygen and Ni atoms within the NiO_6 octahedral. The other oxygen ions do not contribute to the charge transfer mechanism. This suggests Ni-O coupling and that the O^{2-} atoms within the octahedra play a role in facilitating the observed long-range magnetic order. A similar kind of charge-transfer-induced multiferroic property has been observed in many multiferroic systems such as Co_3TeO_6, $HgMn_7O_{12}$, and Cu_2OCl_2, etc. [57–59]. To further corroborate the role of the O atoms, we provide a detailed orbital analysis in Fig. S6 [33]. We also note that there is almost no charge density difference around Te atoms, thus ruling out the role of the Te lone-pair ion contribution to the observed magnetic-order-induced dielectric anomaly.

As the charge density difference in Fig. 5(b) indicates the role of Ni-O interactions, we examined the orbital-projected density of states in detail. Near the Fermi level, the O-p orbitals and Ni-d orbitals have significant contributions, whereas Te has tiny contributions with and without spin-orbit coupling, as shown in Figs. 5(c) and 5(d). The O-p and Ni-d states coincide in both cases, indicating a strong O-p, Ni-d hybridization. The observed p-d hybridization is known as one of the spin-driven mechanisms that could lead to multiferroic properties [54,60]. Surprisingly, ^{125}Te NMR experiments on $NiTe_2O_5$ single crystals predicted strong spin-charge coupled fluctuations which persist well above T_N [31]. This spin-charge coupling occurred via self-hole-doping of Ni^{2+} (d^8), which results in an intermediate charge-transfer state $d^9\underline{L}$; where $\underline{L}$ denotes the oxygen ligand hole. This speculation agrees with our theoretical calculation, where p-d orbital hybridization takes place via charge transfer between the Ni-O atoms, which couples spin-charge degrees of freedom. Near T_N, the divergence of spin-spin correlations further amplified spin-charge coupling that results in strong dielectric anomaly and second-order magnetoelectric coupling in $NiTe_2O_5$. It is essential to mention here that the present magnetoelectric coupling is quite different from that of polar multiferroic Ni_3TeO_6

TABLE III. Quantity of Bader charge transfer calculated through the density functional theory for the AFM and NM cases for the Ni and O atoms along with the difference from AFM to NM cases.

	Charge (e) in AFM case	Charge (e) in NM case	Charge diff (e) = AFM-NM		Charge (e) in AFM case	Charge (e) in NM case	Charge diff (e) = AFM-NM
Ni 1	1.207483	1.141307	0.06618	Ni 5	1.207475	1.141289	0.06619
O 1	−1.11377	−1.09993	−0.01384	O 1	−1.11377	−1.0999	−0.01387
O 2	−1.11859	−1.10394	−0.01465	O 2	−1.11858	−1.10393	−0.01465
O 3	−1.09189	−1.05322	−0.03867	O 3	−1.09141	−1.05275	−0.03866
O 4	−1.05134	−1.0116	−0.03974	O 4	−1.05135	−1.01162	−0.03973
O 5	−1.0914	−1.05275	−0.03865	O 5	−1.09157	−1.05287	−0.0387
O 6	−1.10889	−1.07652	−0.03237	O 6	−1.10886	−1.07651	−0.03235
Ni 2	1.207507	1.141261	0.06625	Ni 6	1.207482	1.141255	0.06623
O 1	−1.11389	−1.09992	−0.01397	O 1	−1.11375	−1.09989	−0.01386
O 2	−1.11857	−1.1039	−0.01467	O 2	−1.11859	−1.10394	−0.01465
O 3	−1.0919	−1.05324	−0.03866	O 3	−1.09139	−1.05272	−0.03867
O 4	−1.05134	−1.0116	−0.03974	O 4	−1.05135	−1.01162	−0.03973
O 5	−1.0914	−1.05274	−0.03866	O 5	−1.0919	−1.05324	−0.03866
O 6	−1.10889	−1.07646	−0.03243	O 6	−1.10886	−1.0765	−0.03236
Ni 3	1.207482	1.141263	0.06622	Ni 7	1.207477	1.141288	0.06619
O 1	−1.11377	−1.10028	−0.01349	O 1	−1.11376	−1.10024	−0.01352
O 2	−1.11859	−1.1039	−0.01469	O 2	−1.10889	−1.07646	−0.03243
O 3	−1.0919	−1.05324	−0.03866	O 3	−1.0914	−1.05274	−0.03866
O 4	−1.05134	−1.0116	−0.03974	O 4	−1.05135	−1.01162	−0.03973
O 5	−1.09139	−1.05272	−0.03867	O 5	−1.0919	−1.05324	−0.03866
O 6	−1.10889	−1.07646	−0.03243	O 6	−1.10886	−1.0765	−0.03236
Ni 4	1.207187	1.140913	0.06627	Ni 8	1.207479	1.141286	0.06619
O 1	−1.11389	−1.10024	−0.01365	O 1	−1.11375	−1.10023	−0.01352
O 2	−1.11858	−1.1039	−0.01468	O 2	−1.11861	−1.10394	−0.01467
O 3	−1.09157	−1.05287	−0.0387	O 3	−1.0914	−1.05275	−0.03865
O 4	−1.05134	−1.0116	−0.03974	O 4	−1.05135	−1.01162	−0.03973
O 5	−1.09141	−1.05275	−0.03866	O 5	−1.09189	−1.05322	−0.03867
O 6	−1.10889	−1.07652	−0.03237	O 6	−1.10886	−1.07651	−0.03235

oxide, where the magnetic exchange striction brings strong electrical polarization and spin-flip-induced magnetoelectric coupling [23]. Despite weaker ME coupling of $NiTe_2O_5$ compared to polar multiferroic Ni_3TeO_6, the present system has its significance such as peculiar dynamic magnetic correlations that persist even in the PM state [31] and charge-transfer-induced second-order magnetoelectric coupling as discussed in Sec. III F.

Further, to check the possibility of Ni-O charge-transfer-induced ferroelectricity, temperature-dependent pyrocurrent measurements were performed (shown in Fig. S7 [33]). The pyrocurrent did not show a peak near T_N for fields up to $E = +0.84\,\mathrm{kV/cm}$. The absence of a pyrocurrent signal indicates the antiferroelectric ordering of the electric dipoles. In fact, as shown in Fig. 5(b), the charge transfer was symmetric between the Ni and O atoms in the NiO_6 octahedral, which may lead to the cancellation of the total electrical dipole moment over the entire unit cell and net-zero electrical polarization. Indeed, four NiO_6 octahedra in the *ab* plane are situated at the center of the edges in a symmetric pattern (i.e., antiferromagnetic arrangement) that might cancel the unit cell's overall dipole moments with net-zero electrical polarization.

F. Symmetry analysis for higher-order magnetoelectric coupling in $NiTe_2O_5$ single crystals

According to a previous neutron study, $NiTe_2O_5$ adopts orthorhombic *Pbnm* crystalline symmetry even at $T = 2$ K. It has an interesting spin structure, with spins preferably aligned along the spin-chain direction FM and between the chain AFM order established. A finite uncompensated magnetic moment (transverse component) forms a stacked, distorted square lattice in the *ab* plane owing to spin canting in the spin-chain direction (right-left-left-right along the spin chain). This unusual spin structure exhibits unconventional critical exponents similar to a two-dimensional magnet, despite the macroscopic 3D magnetic behavior observed from the χ vs T curve (shown in Fig. 1). The adopted magnetic space group, *Pbnm* of $NiTe_2O_5$, does not permit linear ME coupling, as indicated in the Bilbao Crystallographic Server database from crystallography [54]. However, our experimental finding of a robust dielectric anomaly at T_N and the M^2 vs MD scaling indicates the possibility of second-order (higher-order) ME coupling. The second-order ME tensor α_{ijk} ($M_i = \alpha_{ijk}E_jE_k$; direct effect) is possible for the *Pbnm* magnetic space group that supports the experimental outcomes for second-order ME coupling in $NiTe_2O_5$ [61]. The simultaneous evidence

from the magnetic ordering, dielectric, and lattice parameter anomalies indicates the vital role of magnetoelastic phenomena in effectively coupling the magnetic spins with the electrical dipoles at T_N [as shown in Figs. 2(a), 3(a), and 4(c)].

Further, the VASP results for the AFM ground state below T_N provide a strong hybridization between the Ni-*d* and O-*p* states compared to the NM ground state, which justifies the *p*-*d* hybridization's role in the observed signature dielectric anomaly. Furthermore, a clear charge transfer between the Ni-O atoms indicates that the redistribution of local charges owing to magnetic ordering influences the lattice parameters and the local elastic modulus, leading to dielectric signatures at T_N. Further, magnetic field application might induce the spin-flip transition starting from the magnetic field of 4 T, reflected in the dielectric changes and MD coupling in the system. These results suggest the complex nature of the spin-charge-lattice coupling interaction in $NiTe_2O_5$ and agree well with the recent NMR experimental results that predict spin-charge coupling. Although this work highlights the intricate correlations between magnetism and electrical properties in $NiTe_2O_5$, further theoretical and experimental investigations from the optical point of view are highly desirable to unveil deeper insight into this complex spin-charge coupling and its higher-order magnetoelectric coupling.

IV. SUMMARY

Quasi-one-dimensional spin-chain $NiTe_2O_5$ single crystals were successfully grown using the flux method. A dielectric anomaly occurred at T_N, and the scaling of MD% $\propto M^2$ indicated higher-order ME coupling and was consistent with the *Pbnm* magnetic symmetry. The lattice parameter variation from the *T*-dependent XRD signifies the magnetoelastic coupling below T_N. Further, the coupling between spin and electric moments via the magnetoelastic effect below T_N is verified with the theoretical VASP calculation, where the strong *p*-*d* hybridization links the charge transfer between the Ni-*d* and O-*p* orbitals. The concurrent charge redistribution near magnetic ordering and structural anomaly suggests the complex interplay of spin-charge-lattice degrees of freedom in a quasi-one-dimensional spin-chain $NiTe_2O_5$ system.

ACKNOWLEDGMENTS

This work was supported by the Ministry of Science and Technology, Taiwan, under Grants No. MOST 109-2112-M-110-019, No. MOST 108-2112-M-110-014-MY2, No. MOST 110-2112-M-110-008-MY3, No. MOST 110-2112-M-110-013-MY3, and No. MOST 109-2112-M-009-012-MY3.

The authors declare no conflict of interest.

[1] V. Zapf, M. Jaime, and C. D. Batista, Rev. Mod. Phys. **86**, 563 (2014).
[2] D. S. Inosov, Adv. Phys. **67**, 149 (2018).
[3] W. J. L. Buyers, R. M. Morra, R. L. Armstrong, M. J. Hogan, P. Gerlach, and K. Hirakawa, Phys. Rev. Lett. **56**, 371 (1986).
[4] O. V. Maximova, S. V. Streltsov, and A. N. Vasiliev, Crit. Rev. Solid State Mater. Sci. **46**, 371 (2021).
[5] F. D. M. Haldane, Phys. Rev. Lett. **50**, 1153 (1983).
[6] T. M. Rice, Science **298**, 760 (2002).
[7] S. Kimura, K. Kakihata, Y. Sawada, K. Watanabe, M. Matsumoto, M. Hagiwara, and H. Tanaka, Nat. Commun. **7**, 12822 (2016).
[8] Y. S. Tang, J. H. Zhang, L. Lin, R. Chen, J. F. Wang, S. H. Zheng, C. Li, Y. Y. Zhang, G. Z. Zhou, L. Huang, Z. B. Yan, X. M. Lu, D. Wu, X. K. Huang, X. P. Jiang, and J. M. Liu, Phys. Rev. B **103**, 014112 (2021).
[9] R. Moessner and A. P. Ramirez, Phys. Today **59**(2), 24 (2006).
[10] D. C. Cabra, A. O. Dobry, C. J. Gazza, and G. L. Rossini, Phys. Rev. B **103**, 144421 (2021).
[11] J. E. Greedan, J. Mater. Chem. **11**, 37 (2001).
[12] I. A. Sergienko and E. Dagotto, Phys. Rev. B **73**, 094434 (2006).
[13] S. Seki, T. Kurumaji, S. Ishiwata, H. Matsui, H. Murakawa, Y. Tokunaga, Y. Kaneko, T. Hasegawa, and Y. Tokura, Phys. Rev. B **82**, 064424 (2010).
[14] Y. J. Jo, S. Lee, E. S. Choi, H. T. Yi, W. Ratcliff, Y. J. Choi, V. Kiryukhin, S. W. Cheong, and L. Balicas, Phys. Rev. B **79**, 012407 (2009).
[15] R. Chen, J. F. Wang, Z. W. Ouyang, Z. Z. He, S. M. Wang, L. Lin, J. M. Liu, C. L. Lu, Y. Liu, C. Dong, C. B. Liu, Z. C. Xia, A. Matsuo, Y. Kohama, and K. Kindo, Phys. Rev. B **98**, 184404 (2018).
[16] R. Kumar, S. Rayaprol, S. Rajput, T. Maitra, D. T. Adroja, K. K. Iyer, S. K. Upadhyay, and E. V. Sampathkumaran, Phys. Rev. B **99**, 100406(R) (2019).
[17] H. Wu, T. Burnus, Z. Hu, C. Martin, A. Maignan, J. C. Cezar, A. Tanaka, N. B. Brookes, D. I. Khomskii, and L. H. Tjeng, Phys. Rev. Lett. **102**, 026404 (2009).
[18] Y. J. Choi, H. T. Yi, S. Lee, Q. Huang, V. Kiryukhin, and S. W. Cheong, Phys. Rev. Lett. **100**, 047601 (2008).
[19] Y. Wang, G. L. Pascut, B. Gao, T. A. Tyson, K. Haule, V. Kiryukhin, and S. W. Cheong, Sci. Rep. **5**, 12268 (2015).
[20] H. C. Wu, K. D. Chandrasekhar, J. K. Yuan, J. R. Huang, J. Y. Lin, H. Berger, and H. D. Yang, Phys. Rev. B **95**, 125121 (2017).
[21] J. Hwang, E. S. Choi, F. Ye, C. R. DelaCruz, Y. Xin, H. D. Zhou, and P. Schlottmann, Phys. Rev. Lett. **109**, 257205 (2012).
[22] A. G. Christy, S. J. Mills, and A. R. Kampf, Mineral. Mag. **80**, 415 (2016).
[23] Y. S. Oh, S. Artyukhin, J. J. Yang, V. Zapf, J. W. Kim, D. Vanderbilt, and S. W. Cheong, Nat. Commun. **5**, 3201 (2014).
[24] C. R. Feger, G. L. Schimek, and J. W. Kolis, J. Solid State Chem. **143**, 246 (1999).
[25] J. T. S. Irvine, M. G. Johnston, and W. T. A. Harrison, Dalton Trans. **2003**, 2641 (2003).
[26] K. Kohn, K. Inoue, O. Horie, and S. I. Akimoto, J. Solid State Chem. **18**, 27 (1976).
[27] K. Kohn, S. Akimoto, Y. Uesu, and K. Asai, J. Phys. Soc. Jpn. **37**, 1169 (1974).
[28] A. R. M. Iasir, T. Lombardi, Q. Lu, A. M. Mofrad, M. Vaninger, X. Zhang, and D. J. Singh, Phys. Rev. B **101**, 045107 (2020).
[29] A. K. Patel, M. R. Panda, E. Rani, H. Singh, S. S. Samatham, A. Nagendra, S. N. Jha, D. Bhattacharyya, K. G. Suresh, and S. Mitra, ACS Appl. Energy Mater. **3**, 9436 (2020).
[30] J. H. Lee, M. Kratochvilova, H. Cao, Z. Yamani, J. S. Kim, J. G. Park, G. R. Stewart, and Y. S. Oh, Phys. Rev. B **100**, 144441 (2019).
[31] S. H. Baek, J. H. Lee, Y. S. Oh, K. Y. Choi, and B. Büchner, Phys. Rev. B **104**, 214431 (2021).

[32] C. Platte and M. Trömel, Acta Cryst. B **37**, 1276 (1981).
[33] See Supplemental Material at http://link.aps.org/supplemental/10.1103/PhysRevMaterials.6.044409 for the crystal growth flow chart and the detailed refined atomic positions, magnetic, dielectric, and magnetodielectric data of $NiTe_2O_5$ polycrystals along with some of density functional theory calculation data.
[34] P. Hohenberg and W. Kohn, Phys. Rev. **136**, B864 (1964).
[35] G. Kresse and J. Hafner, Phys. Rev. B **47**, 558 (1993).
[36] G. Kresse and J. Furthmüller, Phys. Rev. B **54**, 11169 (1996).
[37] G. Kresse and D. Joubert, Phys. Rev. B **59**, 1758 (1999).
[38] J. P. Perdew, K. Burke, and M. Ernzerhof, Phys. Rev. Lett. **77**, 3865 (1996).
[39] J. Zupan, D. Kolar, and V. Urbanc, Mater. Res. Bull. **6**, 1353 (1971).
[40] I. Živković, K. Prša, O. Zaharko, and H. Berger, J. Phys.: Condens. Matter **22**, 056002 (2010).
[41] R. Sankar, G. J. Shu, B. Karunakara Moorthy, R. Jayavel, and F. C. Chou, Dalton Trans. **42**, 10439 (2013).
[42] T. Katsufuji, S. Mori, M. Masaki, Y. Moritomo, N. Yamamoto, and H. Takagi, Phys. Rev. B **64**, 104419 (2001).
[43] G. A. Samara and P. M. Richards, Phys. Rev. B **14**, 5073 (1976).
[44] M. S. Andújar, S. Y. Vilar, J. Mira, N. Biskup, J. Rivas, S. C. García, and M. A. S. Rodríguez, J. Appl. Phys. **109**, 054106 (2011).
[45] M. S. Seehra, R. E. Helmick, and G. Srinivasan, J. Phys. C: Solid State Phys. **19**, 1627 (1986).
[46] T. Chatterji, G. N. Iles, B. Ouladdiaf, and T. C. Hansen, J. Phys.: Condens. Matter **22**, 316001 (2010).
[47] D. L. Fox, D. R. Tilley, J. F. Scott, and H. J. Guggenheim, Phys. Rev. B **21**, 2926 (1980).
[48] H. C. Wu, K. N. Denisova, D. Menzel, D. C. Kakarla, O. V. Maximova, T. W. Kuo, Z. H. Yang, C. H. Lee, W. H. Li, H. Berger, C. W. Wang, C. K. Chang, Y. C. Chuang, J. Y. Lin, M. Gooch, C. W. Chu, A. N. Vasiliev, and H. D. Yang, Phys. Rev. B **100**, 245119 (2019).
[49] D. C. Kakarla, H. C. Wu, D. J. Hsieh, P. J. Sun, G. J. Dai, J. Y. Lin, J. L. Her, Y. H. Matsuda, L. Z. Deng, M. Gooch, C. W. Chu, and H. D. Yang, Phys. Rev. B **99**, 195129 (2019).
[50] T. D. Sparks, M. C. Kemei, P. T. Barton, R. Seshadri, E. D. Mun, and V. S. Zapf, Phys. Rev. B **89**, 024405 (2014).
[51] K. D. Chandrasekhar, J. K. Murthy, J. Y. Lin, H. C. Wu, W. J. Tseng, A. Venimadhav, and H. D. Yang, Phys. Rev. B **94**, 205143 (2016).
[52] G. Lawes, A. P. Ramirez, C. M. Varma, and M. A. Subramanian, Phys. Rev. Lett. **91**, 257208 (2003).
[53] M. Chandra, S. Yadav, R. J. Choudhary, R. Rawat, A. K. Sinha, M. B. Lepetit, and K. Singh, Phys. Rev. B **98**, 104427 (2018).
[54] M. Fiebig, T. Lottermoser, D. Meier, and M. Trassin, Nat. Rev. Mater. **1**, 16046 (2016).
[55] R. A. Saha, A. Halder, D. Fu, M. Itoh, T. S. Dasgupta, and S. Ray, Inorg. Chem. **60**, 4068 (2021).
[56] K. Cao, R. D. Johnson, F. Giustino, P. G. Radaelli, G. C. Guo, and L. He, Phys. Rev. B **90**, 024402 (2014).
[57] C. H. Lee, C. W.Wang, Y. Zhao, W. H. Li, J. W. Lynn, A. B. Harris, K. Rule, H. D. Yang, and H. Berger, Sci. Rep. **7**, 6437 (2017).
[58] W. T. Chen, C. W. Wang, H. C.Wu, F. C. Chou, H. D. Yang, A. Simonov, and M. S. Senn, Phys. Rev. B **97**, 144102 (2018).
[59] H. C. Wu, J. K. Yuan, K. D. Chandrasekhar, C. H. Lee, W. H. Li, C. W. Wang, J. M. Chen, J. Y. Lin, H. Berger, T. W. Yen, S. M. Huang, C. W. Chu, and H. D. Yang, Mater. Today Phys. **8**, 34 (2019).
[60] S. W. Chen, P. A. Lin, H. T. Jeng, S. W. Fu, J. M. Lee, J. F. Lee, C. W. Pao, H. Ishii, K. D. Tsuei, N. Hiraoka, D. P. Chen, S. X. Dou, X. L. Wang, K. T. Lu, and J. M. Chen, Appl. Phys. Lett. **104**, 082104 (2014).
[61] S. V. Gallego, J. Etxebarria, L. Elcoro, E. S. Tasci, and J. M. P. Mato, Acta Cryst. A **75**, 438 (2019).